Toward high performance of zinc-air battery using hydrophobic carbon foam-based diffusion electrode

Yimai Chen[a], Hui Wang[a], Shan Ji[a,b*], Bruno G. Pollet[c], Rongfang Wang[a**]

[a] College of Chemical Engineering, Qingdao University of Science and Technology, Qingdao, 266042, China

[b] College of Biological, Chemical Science and Chemical Engineering, Jiaxing University, Jiaxing, 314001, China

[c] Department of Energy and Process Engineering, Faculty of Engineering, Norwegian University of Science and Technology (NTNU), Trondheim, NO-7491, Norway

Corresponding authors:

Shan Ji (*): jishan@mail.zjxu.edu.cn, Tel./fax: +86 (0)15024355548

Rongfang Wang (**): rfwang@qust.com.cn, Tel./fax: +86(0)17686458002

Abstract

NaCl is used as template to form porous carbon during the carbonization procedure. It is found that the NaCl amount played an important role in the physical properties of hydrophobic carbon materials. When the current density increases from 0 to 50 mA cm^{-2}, the obtained sample containing zinc-air battery potential decreases from +1.492 V and +1.040 V (*vs.* RHE); a potential drop very close to that of the Pt/C electrode (from +1.489V to +1.043V). It is also found that in continuous discharge operations at 25 mA cm^{-2}, the obtained material exhibits a stable discharge behavior, comparable to Pt/C.

Keywords: N-doped carbon; Porous structure; Hydrophobic; Oxygen reduction reaction; Zinc-air battery.

1. Introduction

Recently, zinc-air battery has attracted great attention as an alternative Electrochemical Storage Device (ESD) to Li-ion battery due to its high energy density and excellent safety features [1]. Because of the sluggish Oxygen Reduction Reaction (ORR) kinetics at the cathode, there is an urgent requirement to develop efficient and low-cost cathode catalysts [2-5]. Although noble metal electrocatalysts show promising electrochemical performance, their scarcity, high cost and poor stability impede the practical applications of zinc-air battery [6, 7]. Therefore, great effort has been focussed on the development of cost-effective catalysts with electrocatalytic activities comparable to noble metallic catalyst ones [8, 9], including the combination of different metals and their doping in carbons [10-12]. Among these catalysts, heteroatoms-doped carbon materials [13, 14], particularly Nitrogen (N)-Doped Carbons, have attracted considerable attention due to their good catalytic activity [15], resulting from the strong electro-negativity of doped nitrogen, favouring the adsorption of O_2 [16-21]. However, currently their electrochemical performance still need to be further improved to meet stringent requirements of the commercialization of zinc-air batteries.

To enhance the catalytic performance of heteroatoms-doped carbons, various strategies for preparing carbons have been adopted to modulate the compositions and structures, including the type and content of heteroatoms, optimized morphology and structure [22]. For example, corrosive chemicals, such as nitrate (NO_3^-) [23-25] and NaOH/KOH [26] have been used to chemically etch the structures for the fabrication of porous materials. However, such a method usually resulted in low yield of product due to the strong reaction between the etching reagent and the material. Templates have

also been used, including *soft* and *hard* ones, to prepare porous materials. For example, surfactant P123 [27] has been commonly used as a *soft* template, while silica microspheres [28, 29] have been often employed as a *hard* template in high temperature carbonization procedures. However, harsh chemicals are required to remove the templates after the porous structures are formed, which make the templating procedures difficult for industrial applications. Another method to form porous structures worth mentionning, is the ionothermal approach, which has been employed since the early 1970's for the preparation of N-doped carbon materials [30]; this is due to the fact that this method uses non-hazardous chemicals and is easy to scale-up over other methods.

Recently, Fechler *et al.* have shown that porous carbon materials can be prepared by carbonizing ionic liquid with inorganic salt at elevated high temperature [31]. During the ionothermal treatment, the eutectic salt acted as template, which can separate the carbon precursor at the nanoscale level and block the growth of chemical bonds. By using an eutectic salt with a relatively low melting point, it was found that low precursor concentrations resulted in fewer sp^3 C-X bonds and higher specific surface areas (SSA) [32, 33]. Furthermore, a high melting point salt, as it is the case for NaCl (mp = 800.9℃), was also used in this method. Among different kinds of inorganic salts with high melting points, the easy-washing characteristic makes NaCl a better choice for synthesizing porous carbon in a large scale. When NaCl was used to form the eutectic salt, it was found that the morphology of the carbon precursor was unaffected by the carbonization process, and the obtained products presented large N-doped amount of higher graphitization degree and better ORR performance when compared with carbon

materials prepared in the absence of NaCl [34].

Inspired by the above investigations, herein, the authors used NaCl as the eutectic salt template to prepare the three-dimensional (3*D*) carbon foam materials using peptone as the precursor [35]. Generally, peptone is composed of small peptides and amino acid [36-38]. The influence of the NaCl amount on the physical properties of the *as*-prepared carbon material and the performance of zinc-air battery was investigated to achieve an optimized NaCl amount. In a zinc-air battery performance experiment, the best N-doped carbon material produced in this study led to rapid dynamic responses together with an Open Cell Potential (OCP) of +1.492 V (*vs.* Zn), a value which was very close to that of commercial Pt/C (+1.489 V (*vs.* Zn)). When the current density reached 50 mA cm^{-2}, the zinc-air battery exhibited a decrease in discharge potential of +1.040 V (*vs.* Zn), comparable to that of Pt/C (+1.043 V *vs.* Zn).

2. Experimental

2.1 Catalyst synthesis

The catalyst synthesis is described in detail as follows: 1 g of peptone (biomass precursor) was mixed and ball-milled in a 0.1 L zircon jar with varied amounts of NaCl (0 g, 5 g, 10 g, 15 g and 20 g) as constructing encapsulator and porogen [34]. The milling process of all samples was carried out with 15 zircon beads (Ø = 0.6 cm) for 6 h at a rotation speed of 550 rpm. After ball-milling, the mixture was transferred into a ceramic crucible and then placed in an inert gas tube furnace. Before heating-up, nitrogen (N_2) was purged into the quartz tube for 30 min, then the temperature was ramped to 900 °C in 360 min and remained at this temperature for 1 h. After that, the

sample was cooled to room temperature. The resultant mixture was immersed in 500 mL H_2O and stirred magnetically for 8 h to wash out any traces of NaCl, and then transferred into 2 M HNO_3 for 24 h to remove inorganic impurities. The obtained product was thoroughly washed with ultrapure water and dried at 80 °C in a vacuum oven. The final products were labelled as NFC-X (X: amount of NaCl).

2.2 Physical characterizations

The morphology of the *as*-prepared carbon materials was studied using Carl Zeiss Ultra Plus scanning electron microscopy (SEM). The water contact angle was measured with an SL200KB apparatus at ambient temperature. The volume of the water in all the measurements was 5 μL. X-ray diffraction (XRD) patterns were generated by a Shimadzu XD-3A XRD spectrometer with a Cu- Kα radiation. The scan was conducted at 2θ values from 5° to 80° at a scan rate of 4° min^{-1}. The specific surface area (SSA) of the samples was measured by the nitrogen adsorption data from 0.05 to 0.25 p p_0^{-1}, and the total pore volume was measured at p p_0^{-1} = 0.99. Furthermore, the Pore Size Distribution (PSD) was obtained using the Quenched Solid State Density Functional Theory (QSDFT) method. Raman spectroscopy was recorded on a Ft-Raman spectrometer (RFS 100, BRU-KER) with a 1,064 nm excitation laser beam wavelength. The intensity of *D* and *G* peaks was gauged by the height from the top point of each band.

2.3 Assembly of the Zn-Air Battery

The battery performance of zinc-air battery was evaluated on a LAND CT2001A test

station. The zinc-air battery was assembled in a two-electrode configuration (using 6 M KOH as electrolyte) with a Zn foil as the active anode material and the *as*-prepared carbon materials as the air cathode. To precisely measure the specific capacity, the Zn foil electrode was tailored to 1 cm^2, and the electrode was polished before each test. The air cathode was prepared by dispersing 9 mg of the *as*-prepared carbon material together with 9 mg of Vulcan XC-72, 9 mg of polymer binder PTFE and 3 mg of carbon black in 300 μL of isopropyl alcohol to form a homogenous slurry. After rolled, cut into slice and dried at 80 °C in an oven, the air cathode mixture was finally pressed onto a Ni foam at a pressure of 20 MPa. The cathode (acting as the reference electrode) made of the commercial Pt/C (20 wt%) was prepared in a similar way.

3. Results and discussion

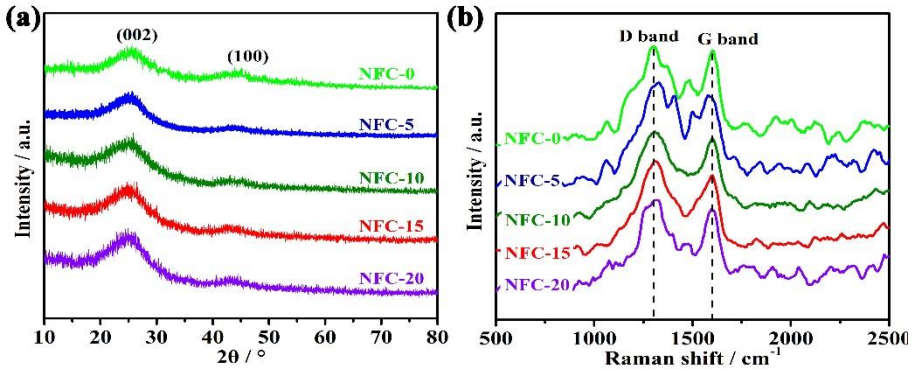

Figure 1. (a) XRD patterns and (b) Raman spectra of obtained samples.

The X-ray diffraction patterns for all the *as*-prepared carbon materials are shown in Figure 1a. In all the XRD patterns, two diffraction peaks at 24.4°-25.8° and 42.9°-44.9° were observed, and were attributed to the hexagonal graphite structures, i.e. (0 0 2) and (1 0 0) planes, respectively [39]. The two peaks are broad, implying their turbostratic structure, resulting from the incomplete graphitization at 900 °C [40]. By using the

well-known *Bragg Equation*, the angle θ corresponding to the (0 0 2) lattice center was used to calculate the graphitic interlayer spacing [41]. It was found that the average graphitic distance increased from 3.45 Å to 3.59 Å (Table 1) with increased amount of NaCl. The highest value of 3.59 Å was obtained in both NFC-15 and NFC-20 samples; a value which was 7.2 % much larger than that of ideal graphite (3.35 Å) [42]. Raman spectroscopy was used to analyze the carbon structure of the resultant samples. As shown in Figure 1b, the *D*-band positioned at around 1,304 cm^{-1} originating from internal defects, which does not exist for pure graphene. From the figure, the *G*-band located at ca. 1,600 cm^{-1} can be ascribed as the graphitic portion vibration [40]. Their intensity ratios I_D/I_G are shown in Table 1. Although all the spectra are similar, increasing the amount of NaCl in the carbonization process resulted in an increase in I_D/I_G ratio with a maximum value of 1.150 for NFC-15. This finding indicates that increasing the amount of NaCl brings about more inner defects in the *as*-prepared carbon materials [43], with an optimum amount of 15 g; however increasing further the amount of NaCl can be detrimental. This observation is also in good agreement with the SSA and PSD results (see later).

Table 1 Graphene spacing, Raman intensity ratio, BET surface area and Total Pore Volume of different carbon catalysts.

sample	**graphene spacing (Å)**	**Raman I_D/I_G ratio**	**BET Surface Area ($m^2\ g^{-1}$)**	**TPV ($cm^3\ g^{-1}$)**
NFC-0	3.45	1.000	72.6	0.067
NFC-5	3.56	1.007	210.4	0.314

NFC-10	3.57	1.056	750.6	1.991
NFC-15	3.59	1.150	950.0	2.521
NFC-20	3.59	1.124	569.9	1.030

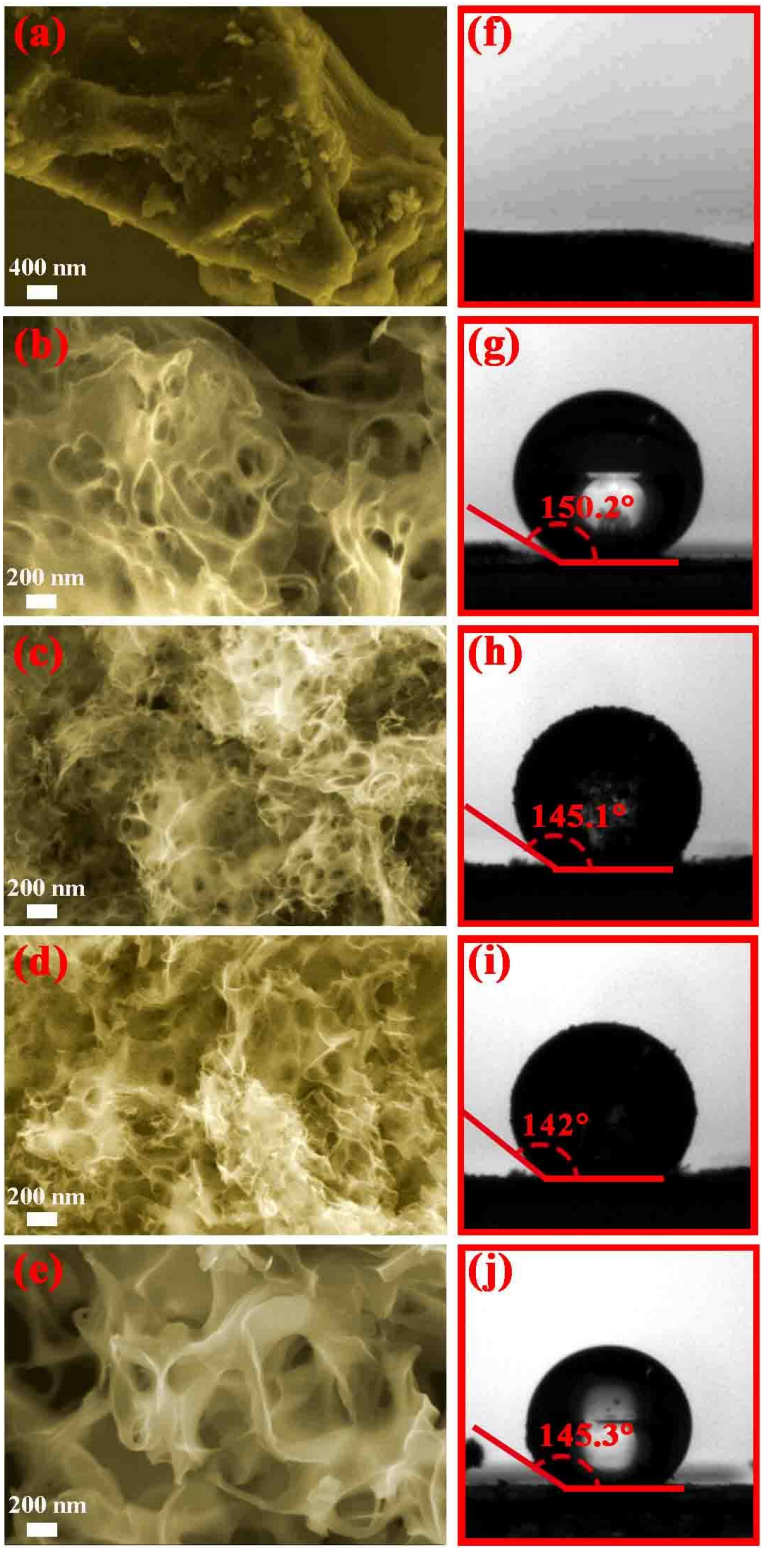

Figure 2. SEM images and contact angles of (a,f) NFC-0, (b,g) NFC-5, (c,h) NFC-10, (d,i) NFC-15, (e,j) NFC-20 respectively.

The morphological changes of the carbon materials prepared using different amounts of NaCl were studied by SEM and are presented in Figure 2. In the absence of salt during synthesis, the NFC-0 (Fig. 2a) sample exhibited conglomerated carbide of dense texture. When 5 g NaCl was added, the carbonization intermediate grew as the *hard* template, until it reached its melting point of 800.9 ℃. The resultant NFC-5 showed sparse foam like structure on the carbon skeleton as presented in Figure 2b. With such a structure, more exposed catalytic active sites can be expected, in contrast with bulk structures e.g. NFC-0. When the NaCl quantity increased to 10 g, it was observed that the interconnected concave or convex on the surface were formed on the NFC-10 sample (Figure 2c). For the NFC-15 sample (Figure 2d), a 3-*D* graphene like material was formed on its surface. In the case of the NFC-20 sample (Figure 2e), a surface with much larger concave and convex of network was formed when compared to the NFC-15 sample. The change in morphology with the amount of NaCl implies that the salt can act as template to form porous structure materials during the carbonization process. Despite significant morphological changes, incremental additions of NaCl resulted in almost the same material yield of 0.09 g for 1 g peptone, more than 0.03 g from the carbonization process in the absence of NaCl. This could be explained to the fixation of the volatile nitrogen, which can be avoided by NaCl crystal[34].

It has been suggested that lower contact angle between water and the ORR catalyst

usually indicates more hydroxyl radicals (*OH) cladding rate around the latter, inhibiting a 4e- process to some extent [44-46]. As a result, hydrophobicity is a required property for highly efficient zinc-air batteries. To explore the affinity of the *as*-prepared carbon materials with water, contact angles were also measured by dropping 5 μL deionized H_2O on the carbon surface. As shown in Figure 2f-j, sample NFC-0 instantaneously absorbed the water droplet, an indication of its wettability, in contrast with the hydrophobic performance of other foam like carbon materials such as: NFC-5, NFC-10, NFC-15 and NFC-20, for which the contact angles were 150.2°, 145.1°, 142°, and 145.3° respectively. Given the fact that the same precursor was used for all *as*-prepared carbon materials, this finding could be due to the difference in geometrical structures of the carbon materials [47]. Furthermore, the change of contact angle for the hydrophobic behaviour is in line with the wettability results previously published on carbon-based materials, whereby the static water contact angle was found to be correlated to the solid surface roughness [48]. It has also been reported that, hydroxyl radicals (*OH), originating from the dissociation of water molecular, acted on the material surface to increase its surface wettability, but in turn inhibited the ORR catalytic reaction [44]. Therefore, in our conditions, the four *as*-prepared foam like carbon materials exhibiting low affinity toward water, should be expected to have high catalytic activity toward ORR.

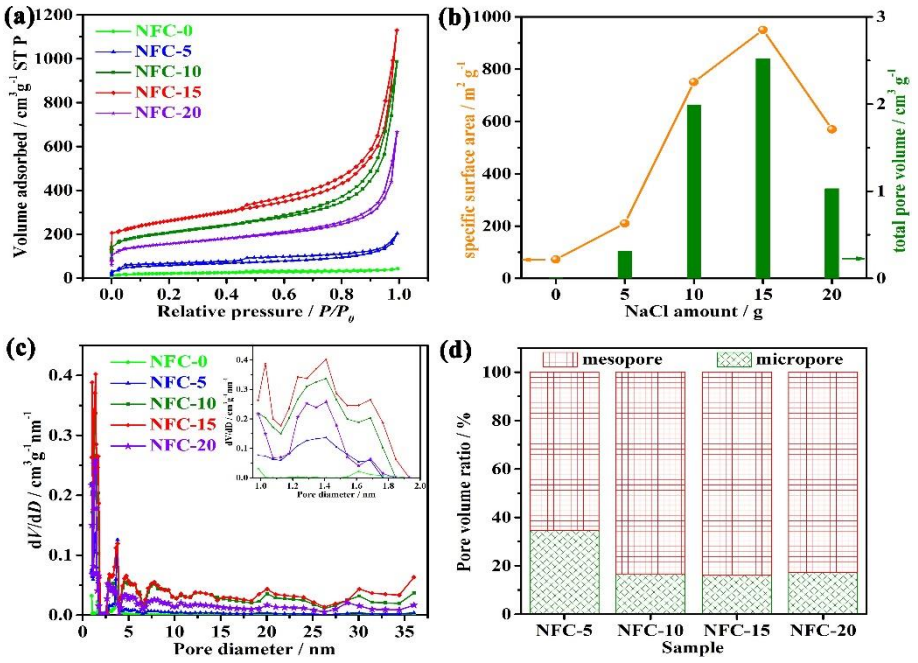

Figure 3. (a) Comparison of N_2 adsorption-desorption isotherms of all samples, and (b) variation trend of SSA and TPV along with various NaCl amounts. (c) Pore size distribution of obtained carbons, the insert plot in PSD graph describes the micropores in detail and (d) the proportion of micro/mespores for NaCl samples.

The nitrogen (N_2) isotherm method was used to evaluate the effect of NaCl on the porosity of the *as*-prepared carbon materials, and the data are illustrated in Figure 3 and Table 1. Isotherms in Figure 3a confirm that the amount of NaCl has great influence on the sample structure, a finding which is in good agreement with the SEM observations. SSA and TPV values of NFC-0 were 72.6 m^2 g^{-1} and 0.07 cm^3 g^{-1} respectively, indicative of the monolithic morphology of NFC-0. The isotherm of the NFC-0 sample hardly shows no uptake with increased P/P_0. In contrast, the isotherms of other foam like carbons exhibited obvious uptakes at relative low pressure, resulting from the presence of a multitude of micropores; the hysteresis loops at relative intermediate to high pressure can be due to abundant mesopores [49]. The hierarchical pore structure

may be induced by the NaCl template and gas emission during the high temperature carbonization process [50]. 5 g of NaCl was used in the process, which could significantly increase the SSA (210.4 m^2 g^{-1}) as well as the TPV (0.31 cm^3 g^{-1}). As shown in Table 1 and Figure 3b, the NFC-10 sample had a SSA of 750.6 m^2 g^{-1} and a TPV of 1.991 cm^3 g^{-1}. For the NFC-15 sample, its SSA was 950.0 m^2 g^{-1}, and TPV reached to an extraordinary value of 2.521 cm^3 g^{-1} [49]. When the amount of NaCl used was 20 g, the SSA and TPV values dropped to 569.9 m^2 g^{-1} and 1.03 cm^3 g^{-1} respectively, which could have resulted from the collapse of small pores and surface structure due to the excess of NaCl. Among all the *as*-prepared samples, the highest value of TPV was greater than 1 cm^3 g^{-1}, a value which is higher than some of other carbon materials reported in the literature [51]. From the PSD of all samples (summarized in Figure 3c), it can be observed that the increase in NaCl in the catalyst fabrication process resulted in an increase in micropores and mesopores simultaneously, but a decrease when its dosage reached 20 g (Figure 3b). It was found that 15 g of NaCl yielded materials of more exposed micropores with larger mesopore volumes. When the ratio of NaCl to peptone (NaCl:peptone) was increased, it was observed that the cross-linked precursor molecules were formed and carbonized along the solid salt to yield a molten template, in turns promoting a steadily increase in pore volume, and thus resulting in the generation of further micro/mesopores (and even larger pores). When the NaCl amount increased to 20 g, the precursor concentration was too low that some pores collapsed, yielding in smaller SSA and TPV values. Accordingly, increased amount of NaCl also resulted in morphology changes as clearly observed in SEM images (Figure 2). Finally,

micropore:mesopore ratio in the final pore system (Figure 3d) indicated that an increase in NaCl led to a mesopore structure (84 % for NFC-15). It was also found that when the NaCl amount was greater than or equal to 10 g, the micropore:mesopore ratio remained at ca. 83.5%, with no large obvious deviations. This type of 3*D* foam like structure formed under the effect of NaCl, the micropore:mesopore ratio was large enough to form an open pore structure, enabling electrocatalysis [49].

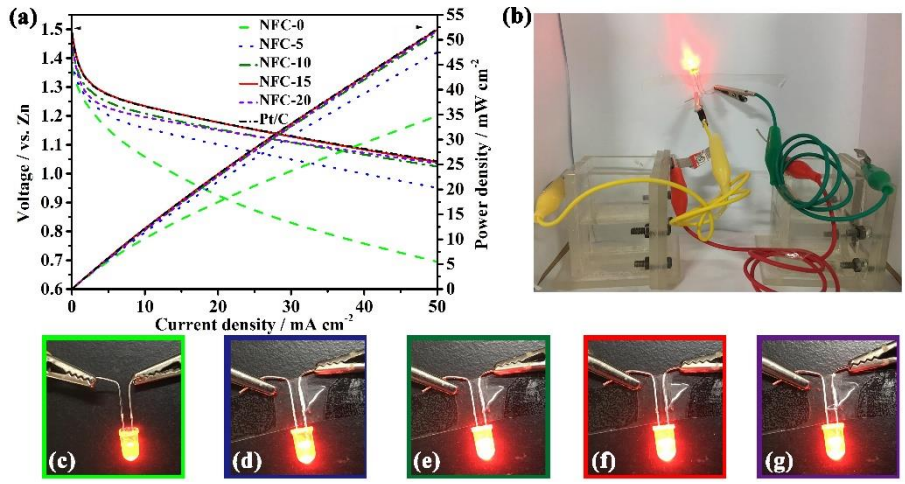

Figure 4. (a) Cell voltage and power density plotted against discharge current for all zinc/air batteries containing NFC-0, NFC-5, NFC-10, NFC-15 and NFC-20 samples. (b) experimental setup of two zinc-air batteries connected in series [containing (c) NFC-0, (d) NFC-5, (e) NFC-10, (f) NFC-15, (g) NFC-20 samples] powering diodes.

For practical applications, all *as*-prepared material samples were used as cathode material in the Zn-air battery experiments, in which a zinc sheet was used as the counter electrode and 6 M KOH as the electrolyte. Figure 4 shows the discharge performances, the current-voltage (I-V) and the corresponding current-power density curves of all the *as*-prepared materials. At first glance, all *as*-prepared materials exhibited high OCP in the Zn-air battery experiments. The OCP for the NFC-15 sample was found to be

+1.492 V (*vs.* Zn), higher than those obtained for NFC-0 (+1.369 V (*vs.* Zn)), NFC-5 (+1.388 V (*vs.* Zn)), NFC-10 (+1.443 V (*vs.* Zn)), and NFC-20 (+1.460 V(*vs.* Zn)); and comparable to that of Pt/C (+1.489 V (*vs.* Zn)). The OCP value of NFC-15 is better than those of reported N/S co-doped carbon derived from sophora [52] and even the complex of transition metal with carbon [53-55]. When the discharge current was 50 mA cm^{-1}, the potentials of all the batteries decrease, and follow the order of: NFC-0 (+0.695 V (*vs.* Zn)) < NFC-5 (+0.950 V (*vs.* Zn)) < NFC-10 (+1.025 V (*vs.* Zn)) < NFC-20 (+1.036 V (*vs.* Zn)) < NFC-15 (+1.040 (*vs.* Zn)) < Pt/C (+1.043 (*vs.* Zn)). It was observed that the NFC-0 sample exhibited the lowest current density and power density among all the *as*-prepared materials, probably due to its poor porous structure. Compared with the NFC-0 sample, the NFC-5 and NFC-10 samples clearly exhibited an increase in current density and power density, resulting from an improved BET surface area and mesopore content as shown in Figure 3. The current density and power density continually increased, and eventually reached maxima for the NFC-15 sample, with values comparable to those of Pt/C. At a discharge current of 50 mA cm^{-2}, the power densities for all air electrodes increased and followed this trend: NFC-0 (34.7 mW cm^{-2}) < NFC-5 (47.5 mW cm^{-2}) < NFC-10 (51.2 mW cm^{-2}) < NFC-20 (51.8 mW cm^{-2}) < NFC-15(52.000 mW cm^{-2}) < Pt/C (52.2 mW cm^{-2}). It was found that the changes of the power density for the carbon-based air electrode were similar to that of the BET surface area and the pore volume, indicating that the two factors play important roles in the catalysis process. Moreover, the discharge performances of the NFC-10, NFC-15, and NFC-20 samples were similar, however their BET surface areas and pore volumes were clearly

different. This finding could be due to their porous structures and similar mesopores to micropores ratio. Generally, zinc-air batteries containing NFC-15 exhibit better performances than others, highlighting the combined importance of porosity and hydrophobicity. To demonstrate the effect of NFC/NFC samples on zinc-air performances, two zinc-air batteries connected in series [containing (c) NFC-0, (d) NFC-5, (e) NFC-10, (f) NFC-15, (g) NFC-20 samples] powered diodes. As the photographic images clearly show in Figure 4, the zinc-air battery containing the NFC-0, NFC-5, NFC-10 and NFC-20 showed weak diode brightness whereas the NFC-15 showed strong diode brightness among all samples.

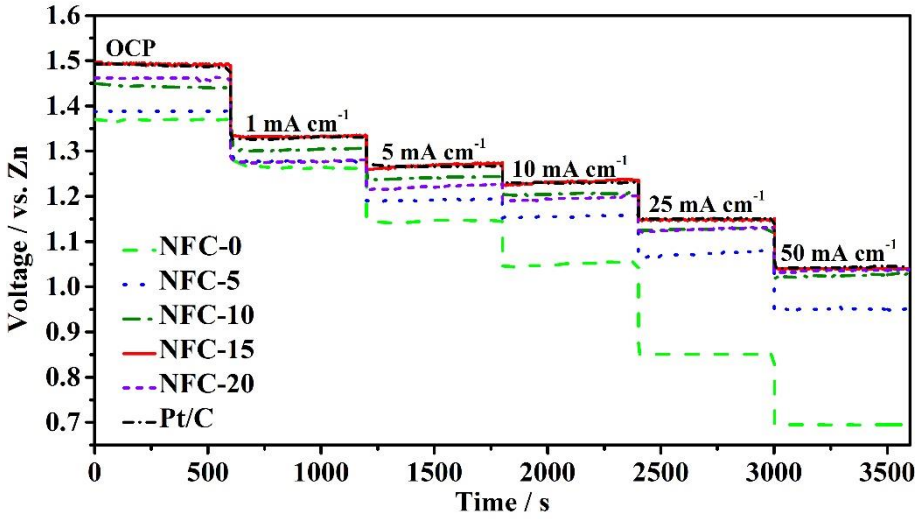

Figure 5. Zn-air battery cell voltage vs. time at various current densities (1 mA cm^{-1}, 5 mA cm^{-1}, 10 mA cm^{-1}, 25 mA cm^{-1} and 50 mA cm^{-1}) using various NFC samples including a commercial 20 wt% Pt/C in 6 m KOH.

The rate performance of batteries is an important factor for advanced electric vehicles. All Zn-air battery containing the *as*-prepared materials exhibited a current step up response at current densities ranging from OCP conditions up 50 mA cm^{-2} as shown in

Figure 5. Within the testing range, NFC-0 zinc-air battery displayed the largest decrease in cell voltage, with OCP values of +1.370 V (vs. Zn) down to +0.695 V (vs. Zn). The drops in cell voltages for the NFC-10, NFC-15, and NFC-20 samples were +0.4 V (vs. Zn), +0.4 V (vs. Zn) and +0.45 V (vs. Zn) respectively at current densities ranging from 0 to 50 mA cm^{-2}. Among all the *as*-prepared Zn-air batteries, the NFC-15 sample exhibited the least decrease, i.e. from +1.492 V (vs. Zn) to +1.040 (vs. Zn), a drop very close to that of the Pt/C condition, +1.489 V (vs. Zn) to +1.043 V (vs. Zn). The results indicated that the air cathode prepared with the NFC-15 sample was robust.

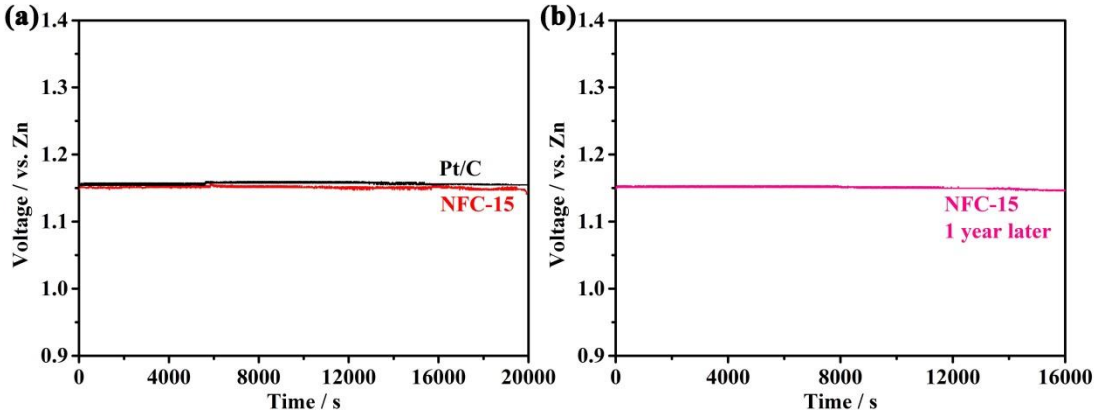

Figure 6. (a) Complete discharge curves for NFC-15 and Pt/C used as zinc-air battery materials and (b) the discharge curve of NFC-15 after NFC-15 was stored in sealed plastic bottle for one year, at 25 mA cm^{-2} in 6 M KOH.

Of all the *as*-prepared zinc-air battery cathode materials, sample NFC-15 displayed the best power as well as rate capability at various current densities, comparable to that of 20 % Pt/C. To explore its stability, an important factor, NFC-15 and Pt/C were both subjected to continuous discharge operations at 25 mA cm^{-2} for 20,000 seconds. As shown in Figure 6a, the NFC-15 sample displayed a stable discharge rate over 20,000s, comparable to that of Pt/C. In our conditions and from our findings, it can be postulated

that NFC-15 could replace Pt/C in zinc/air battery. After NFC-15 has been stored in a sealed plastic bottle for one year, no decrement was observed in Figure 6b, which further verified its excellent stability.

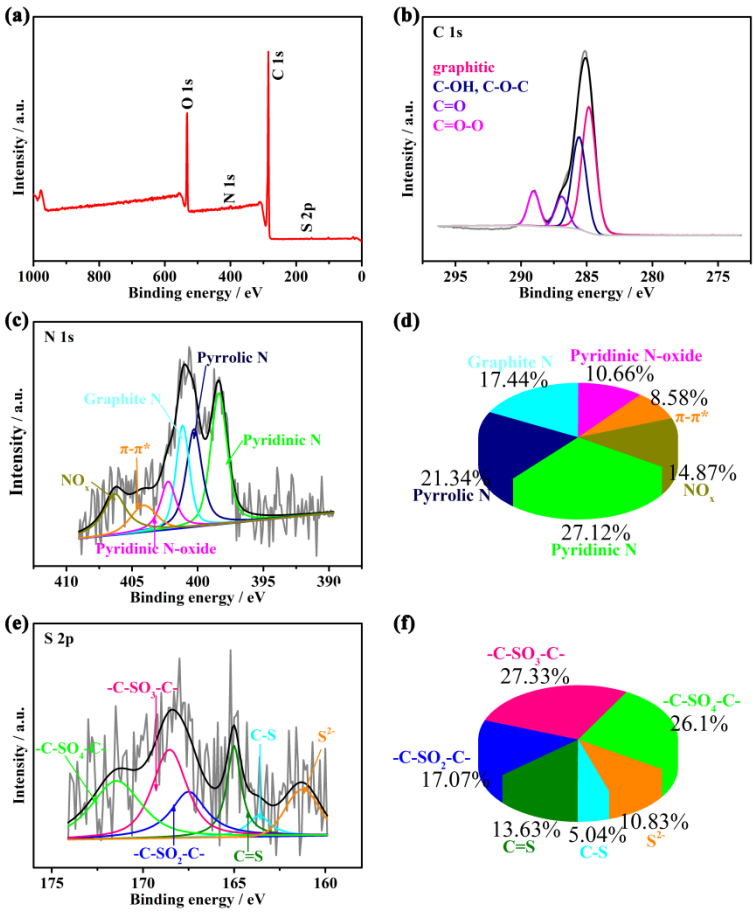

Figure 7. XPS (a) full spectra, high resolution scans of (b) C *1s* (c) N *1s* (e) S *2p*, each chemical type content of (d) N and (f) S for the NFC-15 sample.

To clarify the origin of the catalytic activity of the NFC-15 sample, XPS elemental analyses were conducted. According to the full spectrum, shown in Figure 7a, the NFC-15 sample is composed of C, O, N and S (C 82.57 at.% and N 0.64 at.%). Furthermore, trace amount of S was also observed, which has been shown in previous studies to yield a high selectivity towards ORR and enhanced zinc-air battery performances [56]. It can be expected that the combination of N,S-doped sites and edge-rich holes may induce

fast electrode kinetics for ORR performance. The presence of O element in NFC-15 samples indicates oxidation in the carbonization process, caused by residual oxygen substances. However, it has been reported in the literature that the oxidized species does not affect significantly the catalytic properties of carbon materials [57]. All elemental spectra were also used to achieve a deeper understanding of the chemical states of each element in the sample. As illustrated in Figure 7b, the C 1*s* region can be fitted into four peaks, namely: graphitic (+284.8 eV), C-OH, C-O-C (+285.6 eV), C=O (+286.9 eV) and O=C-O (+289 eV). As can be observed, among the four species, the main part is the graphitic C. Detailed analysis of N 1*s* fine spectra in Figure 7c confirms its incorporation into the sp^2 network. Indeed, there are six N-species, pyridinic-N ca. +398.3 eV, pyrrolic-N ca. +399.9 eV, graphitic-N (N-Q) ca. +401.1 eV, pyridinic N-oxide ca. +402.3 eV, π-π* satellite ca. +404.4 eV, and entrapped NO_x ca. +406.3 eV [56]. Quantification for each N chemical composition is shown in Figure 7d. Among the different chemical states of N 1*s*, pyridinic-N provides a pair of electrons to bond with the *p*-conjugated rings, with the pyrrolic-N known to be good at donating electrons. Graphitic-N, especially that on the edge, has been proven to bring about lower overpotential for ORR, resulting in better performances than pyridinic-N [49, 58, 59]. It is also worth noting that NaCl promotes NO_X to more stable valence states (pyridinic/graphitic nitrogen and thiophenic sulfur), as shown in Figure 7d and 7f [34].

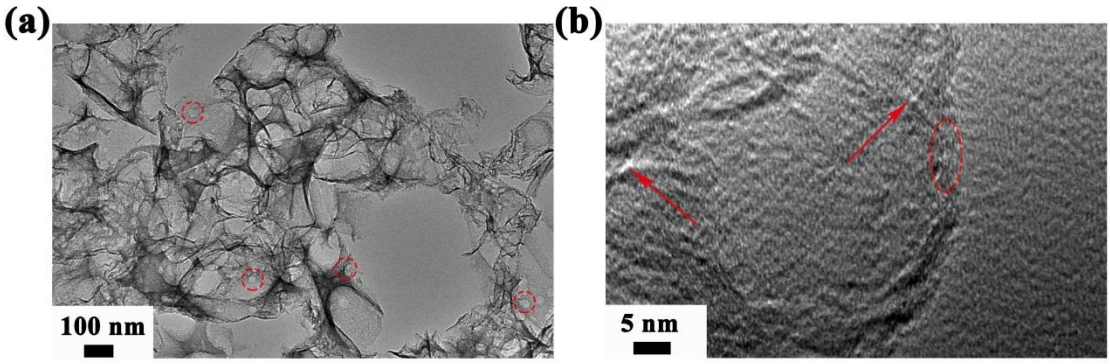

Figure 8. TEM images NFC-15.

Transmission electron microscopy (TEM) was also performed to observe its detail structure (Figure 8). TEM of Figure 8a indicates that the obtained carbon material consists of graphene-like sheets with large amounts of mesopores, even some macropores and plenty of topical defects (marked by red circles), and these sheets are interconnected with each other. There are also lots of square-like defects on these sheets, a reflection of NaCl's face-centered cubic structure. While the HRTEM images in Figure 8b show a high density of micropores in the carbon network (marked with red arrows). Besides, no orderly lattice fringes were observed in the HRTEM image, indicating lattice fringes were distorted in the obtained carbon due to the relatively low carbonization temperature. As shown in the oval circle in Figure 8b, the graphene-like sheet for NFC-15 consists of ca. two layers.

Based upon the above results, three properties of the NFC-15 sample may account for its overall high electrochemical performance. Firstly, N and S atoms are present in NFC-15. These two types of heteroatoms provide active sites for ORR. Moreover, the synergistic effect of the two N and S dopants could also result in an enhanced ORR performance [56]. Secondly, the open porous structure make the electrolyte, in theory,

reach the inner surface of the NFC-15 sample through the rich mesopores, allowing oxygen molecules and hydroxyl ions (OH^-) in the electrolyte access to the interior of the active site, in turns improving the ORR process [60, 61]. Thirdly, hydrophobicity of the NFC-15 sample helps in the ORR process by dominantly catalyzing electron acceptor redox reaction resulting from inhibiting parasitic reactions such as the Oxygen Evolution Reaction (OER) [44, 45].

4. Conclusions

It was found that 3*D*-foam like N,S-doped graphene architectures can been tuned with NaCl. Peptone was employed as the C, N and S source and carbonized at 900 ℃ for 60 min. 15 g NaCl was found to be the optimum salt amount yielding materials possessing 3*D*-foam like structures with the largest BET surface area (950.0 $m^2 g^{-1}$) and TPV (2.251 $cm^3 g^{-1}$), at a micropore:mesopore ratio of 83.4 %. The resultant NFC-15 sample presented the best zinc-air performance among all *as*-prepared cathode materials. It was observed that the NFC-15 sample had the largest mesopore volume, high content of pyridinic and graphite N, and great hydrophobicity leading to a superior zinc-air battery performance comparable to that of Pt/C. It was also found that the NFC-15 sample exhibited a stable discharge rate, at a constant current density, in which the cell voltage was almost *on par* to that of Pt/C.

Acknowledgements

The authors would like to thank the National Natural Science Foundation of China (51661008 and 21766032) for financially supporting this work.

References

[1] D. Yang, L. Zhang, X. Yan, X. Yao, Small Methods, 1 (2017) 1700209.

[2] M.A. Rahman, X. Wang, C. Wen, Journal of the Electrochemical Society, 160 (2013) A1759-A1771.

[3] P. Ingale, M. Sakthivel, J.F. Drillet, Journal of the Electrochemical Society, 164 (2017) H5224-H5229.

[4] B. Jiang, C. Li, V. Malgras, M. Imura, S. Tominaka, Y. Yamauchi, Chemical Science, 7 (2016) 1575-1581.

[5] C. Li, T. Sato, Y. Yamauchi, Angewandte Chemie, 125 (2013) 8208-8211.

[6] W. Wang, R. Wang, S. Ji, H. Feng, H. Wang, Z. Lei, J. Power Sources, 195 (2010) 3498-3503.

[7] J. Ding, S. Ji, H. Wang, J. Key, D.J.L. Brett, R. Wang, Journal of Power Sources, 374 (2018) 48-54.

[8] Y. Ma, R. Wang, H. Wang, J. Key, S. Ji, J. Power Sources, 280 (2015) 526-532.

[9] Y. Ma, H. Wang, J. Key, V. Linkov, S. Ji, X. Mao, Q. Wang, R. Wang, International Journal of Hydrogen Energy, 39 (2014) 14777-14782.

[10] Y. Guo, J. Tang, J. Henzie, B. Jiang, H. Qian, Z. Wang, H. Tan, Y. Bando, Y. Yamauchi, Materials Horizons, 4 (2017) 1171-1177.

[11] H. Tan, Y. Li, X. Jiang, J. Tang, Z. Wang, H. Qian, P. Mei, V. Malgras, Y. Bando, Y. Yamauchi, Nano Energy, 36 (2017) 286-294.

[12] Y. Guo, J. Tang, H. Qian, Z. Wang, Y. Yamauchi, Chemistry of Materials, 29 (2017) 5566-5573.

[13] X. Zhang, Q. Huang, F. Deng, H. Huang, Q. Wan, M. Liu, Y. Wei, Applied Materials Today, 7 (2017) 222-238.

[14] X. Zhang, Q. Huang, M. Liu, J. Tian, G. Zeng, Z. Li, K. Wang, Q. Zhang, Q. Wan, F. Deng, Y. Wei, Applied Surface Science, 343 (2015) 19-27.

[15] Y. Shi, M. Liu, F. Deng, G. Zeng, Q. Wan, X. Zhang, Y. Wei, Journal of Materials Chemistry B, 5 (2017) 194-206.

[16] R. Wang, H. Song, H. Li, H. Wang, X. Mao, S. Ji, Journal of Power Sources, 278 (2015) 213-217.

[17] R. Wang, H. Wang, T. Zhou, J. Key, Y. Ma, Z. Zhang, Q. Wang, S. Ji, Journal of Power Sources, 274 (2015) 741-747.

[18] R. Wang, K. Wang, Z. Wang, H. Song, H. Wang, S. Ji, Journal of Power Sources, 297 (2015) 295-301.

[19] X. Ma, S. Feng, S. Ji, International Journal of Electrochemical Science, 12 (2017) 7869-7876.

[20] Q. Huang, M. Liu, L. Mao, D. Xu, G. Zeng, H. Huang, R. Jiang, F. Deng, X. Zhang, Y. Wei, Journal of Colloid and Interface Science, 499 (2017) 170-179.

[21] Q. Huang, M. Liu, J. Chen, Q. Wan, J. Tian, L. Huang, R. Jiang, Y. Wen, X. Zhang, Y. Wei, Applied Surface Science, 419 (2017) 35-44.

[22] M. Liu, G. Zeng, K. Wang, Q. Wan, L. Tao, X. Zhang, Y. Wei, Nanoscale, 8 (2016) 16819-16840.

[23] X. Dong, N. Hu, L. Wei, Y. Su, H. Wei, L. Yao, X. Li, Y. Zhang, Journal of Materials Chemistry A, 4 (2016) 9739-9743.

[24] T. Ouyang, K. Cheng, Y. Gao, S. Kong, K. Ye, G. Wang, D. Cao, Journal of Materials Chemistry A, 4 (2016) 9832-9843.

[25] Y. Chen, H. Wang, S. Ji, B.G. Pollet, R. Wang, Materials Research Bulletin, 104 (2018) 134-142.

[26] K.N. Chaudhari, M.Y. Song, J.-S. Yu, Small, 10 (2014) 2625-2636.

[27] H. Yan, Chemical Communications, 48 (2012) 3430-3432.

[28] H. Wang, K. Wang, J. Key, S. Ji, V. Linkov, R. Wang, J. Electrochem. Soc., 161 (2014) H637-H642.

[29] H. Zhao, Y.-P. Zhu, L. Ge, Z.-Y. Yuan, International Journal of Hydrogen Energy, 42 (2017) 19010-

19018.
[30] E. Ota, S. Inoue, M. Horiguchi, S. Otani, Bulletin of the Chemical Society of Japan, 52 (1979) 3400-3406.
[31] N. Fechler, T.-P. Fellinger, M. Antonietti, Advanced Materials, 25 (2013) 75-79.
[32] Y. Chen, S. Huo, H. Wang, in Engineering morphology and porosity of N,S-doped carbons by ionothermal carbonisation for increased catalytic activity towards oxygen reduction reaction, pp. 530-535, Institution of Engineering and Technology, (2018).
[33] Y. Chen, H. Wang, F. Liu, H. Gai, S. Ji, V. Linkov, R. Wang, Chemical Engineering Journal, 353 (2018) 472-480.
[34] W. Ding, L. Li, K. Xiong, Y. Wang, W. Li, Y. Nie, S. Chen, X. Qi, Z. Wei, Journal of the American Chemical Society, 137 (2015) 5414-5420.
[35] Y. Shi, R. Jiang, M. Liu, L. Fu, G. Zeng, Q. Wan, L. Mao, F. Deng, X. Zhang, Y. Wei, Materials Science and Engineering: C, 77 (2017) 972-977.
[36] L. Huang, M. Liu, H. Huang, Y. Wen, X. Zhang, Y. Wei, Biomacromolecules, 19 (2018) 1858-1868.
[37] X. Zhang, S. Wang, L. Xu, L. Feng, Y. Ji, L. Tao, S. Li, Y. Wei, Nanoscale, 4 (2012) 5581-5584.
[38] M. Liu, J. Ji, X. Zhang, X. Zhang, B. Yang, F. Deng, Z. Li, K. Wang, Y. Yang, Y. Wei, Journal of Materials Chemistry B, 3 (2015) 3476-3482.
[39] H. Wang, H. Da, S. Ji, S. Liao, R. Wang, J. Electrochem. Soc., 160 (2013) H266-H270.
[40] T. Zhou, H. Wang, S. Ji, V. Linkov, R. Wang, J. Power Sources, 248 (2014) 427-433.
[41] A. Mulyadi, Z. Zhang, M. Dutzer, W. Liu, Y. Deng, Nano Energy, 32 (2017) 336-346.
[42] H. Wang, D. Mitlin, J. Ding, Z. Li, K. Cui, Journal of Materials Chemistry A, 4 (2016) 5149-5158.
[43] R. Wang, H. Da, H. Wang, S. Ji, Z. Tian, J. Power Sources, 233 (2013) 326-330.
[44] K.A. Stoerzinger, W.T. Hong, G. Azimi, L. Giordano, Y.-L. Lee, E.J. Crumlin, M.D. Biegalski, H. Bluhm, K.K. Varanasi, Y. Shao-Horn, The Journal of Physical Chemistry C, 119 (2015) 18504-18512.
[45] R. Thimmappa, A.R. Kottaichamy, S. Aralekallu, M. Gautam, S.P. Shafi, Z.M. Bhat, M.O. Thotiyl, Journal of Physical Chemistry C, 121 (2017) 3707-3713.
[46] Y. Chen, H. Wang, S. Ji, R. Wang, Catalysis Communications, 107 (2018) 29-32.
[47] J. Li, Z. Zhao, D. Li, H. Tian, F. Zha, H. Feng, L. Guo, Nanoscale, 9 (2017) 13610-13617.
[48] E. Singh, Z. Chen, F. Houshmand, W. Ren, Y. Peles, H.-M. Cheng, N. Koratkar, Small, 9 (2013) 75-80.
[49] J. Pampel, T.-P. Fellinger, Advanced Energy Materials, 6 (2016) 1502389-n/a.
[50] J. Qin, C. He, N. Zhao, Z. Wang, C. Shi, E.-Z. Liu, J. Li, ACS Nano, 8 (2014) 1728-1738.
[51] B. Lu, L. Hu, H. Yin, X. Mao, W. Xiao, D. Wang, International Journal of Hydrogen Energy, 41 (2016) 18713-18720.
[52] X. Li, H. Xu, ChemistrySelect, 3 (2018) 10624-10629.
[53] L. Song, T. Wang, L. Li, C. Wu, J. He, Applied Catalysis B: Environmental, (2018).
[54] Q. Qin, P. Li, L. Chen, X. Liu, ACS Applied Materials & Interfaces, (2018).
[55] F. Kong, X. Fan, A. Kong, Z. Zhou, X. Zhang, Y. Shan, Advanced Functional Materials, 0 1803973.
[56] Y. Chen, H. Wang, S. Ji, W. Lv, R. Wang, Materials, 10 (2017) 1366.
[57] Y. Chen, S. Ji, H. Wang, V. Linkov, R. Wang, International Journal of Hydrogen Energy, 43 (2018) 5124-5132.
[58] C. Tang, H.-F. Wang, X. Chen, B.-Q. Li, T.-Z. Hou, B. Zhang, Q. Zhang, M.-M. Titirici, F. Wei, Advanced Materials, 28 (2016) 6845-6851.
[59] G. Ferrero, K. Preuss, A. Fuertes, M. Sevilla, M.-M. Titirici, Journal of Materials Chemistry A, 4 (2016) 2581-2589.

[60] R. Wang, T. Zhou, H. Wang, H. Feng, S. Ji, Journal of Power Sources, 269 (2014) 54-60.
[61] R. Wang, T. Zhou, H. Li, H. Wang, H. Feng, J. Goh, S. Ji, Journal of Power Sources, 261 (2014) 238-244.